Effect of chaos on two-dimensional spin transport

Chen-Rong Liu,[1] Xian-Zhang Chen,[1] Hong-Ya Xu,[2] Liang Huang,[1,*] and Ying-Cheng Lai[2,3]

[1]*School of Physical Science and Technology, and Key Laboratory for Magnetism and Magnetic Materials of MOE, Lanzhou University, Lanzhou, Gansu 730000, China*

[2]*School of Electrical, Computer, and Energy Engineering, Arizona State University, Tempe, Arizona 85287, USA*

[3]*Department of Physics, Arizona State University, Tempe, Arizona 85287, USA*

(Received 21 May 2018; revised manuscript received 1 September 2018; published 24 September 2018)

The role of classical dynamics in spin transport is an intriguing problem from the point of view of classical-quantum correspondence, as spin is a purely relativistic quantum mechanical variable with no classical counterpart. Nevertheless, due to spin-orbit coupling (generally referred to as the relativistic interaction of a particle's spin with its motion inside a potential) and because the orbital motion does have a classical correspondence, the nature of the classical dynamics can affect spin. A basic transport structure is quantum dots, whose geometrical shape can be chosen to lead to characteristically distinct classical behaviors ranging from integrable dynamics to chaos. Whether and how classical chaos can affect spin transport and if the effect can be exploited for applications in spintronics are thus issues of both fundamental and practical interest. Here we report results from systematic, full quantum computations of spin transport through quantum dots hosting different types of classical dynamics. Our main finding is that chaos can play orthogonal roles in affecting spin polarization, depending on the relative strength of the spin-orbit coupling. For weak coupling with a characteristic interaction length much larger than the system size, chaos can be beneficial to preserving spin polarization. In the strong coupling regime where the interaction length is smaller than the system dimension, chaos typically destroys spin polarization. We develop a semiclassical theory to understand these phenomena and point out their implications and potential applications in developing spintronic devices.

DOI: 10.1103/PhysRevB.98.115305

I. INTRODUCTION

Spin transport, the spin-dependent electron transport in mesoscopic systems, is fundamental to condensed matter physics [1–3] and the development of energy efficient electronics [1,2] such as spintronics. Advances in experimental techniques [4,5] have made it possible to uncover, understand, and exploit a variety of phenomena related to spin transport. In terms of basic physics, how to generate polarized spin currents from unpolarized electron injections, i.e., spin rectification [6], and how to preserve spin polarization during electronic transport [1] are issues of current interest [3,7]. The main point of this paper is that, under certain circumstances, classical chaos can either help to preserve or destroy spin polarization.

Spin transport represents a subclass of phenomena in the broad context of electronic transport [8], a field that has been relatively well developed. To explain the motivation behind our work, we briefly describe the pertinent problem of the interplay between classical dynamics and quantum transport. When electrons traverse a nanostructure, e.g., a quantum dot, universal conductance fluctuations can arise [9–14]. If the underlying classical dynamics are integrable or mixed in the sense that there are both Kolmogorov-Arnold-Moser (KAM) tori and chaotic components in the phase space [15], sharp, Fano-type of resonances in the conductance curve of interest (e.g., conductance versus the Fermi energy or the strength of an external magnetic field) can arise, but the resonances are smoothed out when the classical dynamics are fully chaotic [13,16–22]. The ability for classical chaos to suppress or even eliminate resonances has led to the proposal of the control scheme to mitigate conductance fluctuations through chaos [23,24]. For electronic or charge transport, it seems quite natural to investigate the interplay between classical dynamics and quantum characteristics as, in this context, a classical-quantum correspondence exists.

Spin is a relativistic quantum characteristic with no classical counterpart. Intuitively, there is no direct classical correspondence to spin transport. A question is then: is it meaningful to study the interplay between classical dynamics and spin transport? The answer is affirmative, thanks to Rashba spin-orbit coupling [25–31]—a relativistic type of interaction of a particle's spin with its orbital motion inside a potential. Because the orbital motion in general has a classical correspondence, the nature of the classical dynamics can affect spin transport.

Depending on whether the injected electrons are spin unpolarized or polarized, chaos can have a characteristically distinct effect on spin polarization. To explain these results, we consider a two dimensional system. In particular, for unpolarized injection, if the system is invariant under the symmetric operation $\boldsymbol{r} \leftrightarrow -\boldsymbol{r}$, where $\boldsymbol{r}$ is the position vector in the (x, y) plane, the z-component of spin polarization must be zero [32]. From the semiclassical point of view, if initially electrons are spin-unpolarized, the precession caused by

*huangl@lzu.edu.cn

spin-orbit coupling of an electron with spin $\boldsymbol{P}$ is opposite to that of an electron with spin $-\boldsymbol{P}$. As a result, at any time the spins of the two electrons are in exactly opposite directions and thus cancel each other completely, giving rise to zero total spin polarization. Quantum mechanically, there can be residuals of the x or y component of spin polarization. In this case, classical chaos or edge roughness of the underlying quantum confinement structure can reduce the cancellation of the spin of the pair of electrons with initial opposite spins, leading to an enhancement in the residual polarization [33,34].

For spin polarized injection, a related phenomenon is that, classical chaos can preserve the polarization [35]. In particular, in Ref. [35], the authors investigated spin relaxation in two-dimensional electron systems with an antidot structure through Monte Carlo simulations in the semiclassical regime, in which the electron motion can be mapped to that in a closed quantum confinement with the geometry of a chaotic billiard with the degree of chaos determined by the geometric parameters. It was found that chaos can suppress the relaxation of spin polarization by increasing the relaxation time or, for a given relaxation time, strengthening the amount of spin polarization. However, there are circumstances under which chaos can play the opposite role to suppress spin polarization. For example, path-integral based simulations of spin evolution controlled by Rashba spin-orbit interaction in the semiclassical regime for chaotic and integrable (circular) quantum confinements revealed [36] that chaos can make the spin polarization approach zero. However, classically integrable dynamics can lead to a constant, nonzero residual polarization value—a result confirmed by a full quantum analysis.

Most previous works focused on closed systems in the semiclassical regime [35,36]. The purpose of this paper is to carry out full quantum computations and analysis of spin transport in open quantum dot systems. Our focus is on spin polarized injection and the effect of classical chaos on quantum spin transport in 2D mesoscale quantum dots. To be comprehensive, we consider four types of quantum dots that exhibit different degree of chaos in the classical limit. In each case, polarized spin current is injected into the left side of the dot. We use the spin-resolved Usuki recursive scattering matrix method [37–39] to calculate and analyze the transport through the dot region with Rashba spin-orbit coupling. The calculation gives the degree of spin polarization at the right side and the spin-resolved Fano factor of shot noise. As the system changes from being integrable to mixed and becomes fully chaotic in the classical limit, the Fano factor increases systematically, indicating a stronger degree of mixing of different transmitting channels. For spin polarization, there are two distinct cases: the characteristic spin-orbit interaction length is much larger than or comparable/smaller than the device size, corresponding to the weak or strong coupling regime, respectively. In the weak coupling regime, chaos is beneficial to preserving spin polarization, but in the strong coupling regime, chaos will diminish spin polarization. We provide a physical understanding of these phenomena through analyzing the semiclassical spin precession along the classical orbits. In particular, the generic difference between an integrable/mixed and a chaotic system is that the former has stable periodic orbits while for the latter, all periodic orbits are unstable and are scattered in phase space,

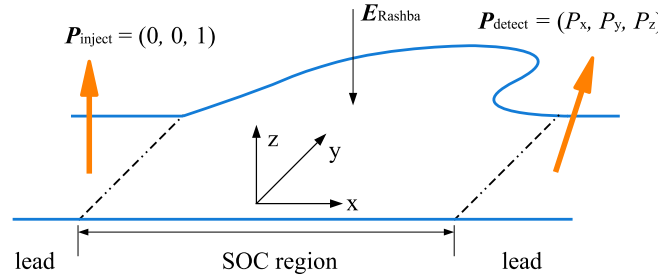

FIG. 1. Schematic illustration of spin transport in two dimensions. The Rashba spin-orbit coupling (SOC) is induced by an external electrical field $\boldsymbol{E}_{\text{Rashba}}$ in the SOC region.

so that the direction of spin polarization vector can change in a random manner. In the weak coupling regime, for an integrable or mixed system, a trajectory reflects from the boundary in a regular way, so spin polarization tends to be weakened systematically. For a chaotic system, while the spin polarization vector changes randomly, the amplitude of the change is small, mimicking a small step random walk. On average, after many reflections (walks), spin polarization can be preserved. In the strong coupling regime, for an integrable/mixed system, spin polarization tends to vary in a regular manner: it decreases to zero and then increases in the opposite direction, and so on. For a chaotic system, as the magnitude of the change in spin polarization vector is larger, the randomness in the rotating axis deteriorates the vector quickly, especially when there are multi-transmitting channels, leading to destruction of spin polarization.

In Sec. II, we describe the device model and provide formulas for quantities such as spin-resolved transmission, spin-polarization vector, and the Fano factor characterizing the shot noise of the system. In Sec. III, we present results on the effect of chaos on spin transport. In Sec. IV, we provide a semiclassical explanation of the main results based on examining and comparing the structure of the Poincaré section of the classical trajectories for different types of classical dynamics. A discussion is presented in Sec. V.

II. SPIN TRANSPORT IN TWO DIMENSIONS

Figure 1 illustrates a general two-terminal spin transport system, which consists of a left lead, a Rashba spin-orbit coupling region (or cavity), and a right lead. The Rashba spin-orbit interaction is induced by an external electric field $\boldsymbol{E}_{\text{Rashba}}$ in the cavity region. The electron in the cavity is confined by an electric potential that is infinite outside but vanishes inside the cavity and the lead region. The boundary of the cavity can be chosen to generate integrable, mixed, or chaotic dynamics in the classical limit. Polarized electrons with spin polarization $\boldsymbol{P}_{\text{inject}} = (0, 0, 1)$ are injected from the left lead into the cavity [40,41]. They undergo scattering inside the cavity and finally exit from the right lead with spin polarization $\boldsymbol{P}_{\text{detect}} = (P_x, P_y, P_z)$. In general, both Rashba interaction and the geometrical shape of the cavity can affect the electron motion, with the corresponding Hamiltonian given by

$$\hat{\mathcal{H}} = \frac{\hat{\boldsymbol{p}}^2}{2m^*}\sigma_0 + \frac{\boldsymbol{\alpha}}{\hbar}\cdot(\hat{\boldsymbol{\sigma}} \times \hat{\boldsymbol{p}}), \tag{1}$$

where σ_0 is the 2×2 unit matrix, $\hat{\boldsymbol{\sigma}}=(\sigma_x,\sigma_y)$ are the Pauli matrices, m^* is the electron's effective mass inside the cavity, $\boldsymbol{\alpha}=[\hbar/(2m^*c)^2]\nabla U=-[\hbar/(2m^*c)^2]\boldsymbol{E}_{\text{Rashba}}$ characterizes the strength of Rashba spin-orbit coupling, which can be obtained [42] by expanding the Dirac equation in terms of v/c. For a given Fermi energy, the wavefunction inside the ideal leads attached to both sides of the cavity can be expressed as a linear combination of the spin-polarized conducting channels $|n\sigma\rangle=|n\rangle\otimes|\sigma\rangle$, with n and σ being the channel and spin indices, respectively. For an incoming state with certain channel and spin indices, the outgoing state can be expanded by $|n\sigma\rangle$ of the right lead, i.e.,

$$|\text{in}\rangle=|n\rangle\otimes|\sigma\rangle, \tag{2}$$

$$|\text{out}\rangle=\sum_{n',\sigma'}\boldsymbol{t}_{n'n,\sigma'\sigma}|n'\rangle\otimes|\sigma'\rangle. \tag{3}$$

The square modulus of the expansion coefficients $\boldsymbol{t}_{n'n,\sigma'\sigma}$ gives the probability for a spin-σ incoming channel $|n\rangle$ from the left lead to scatter into a spin-σ' channel $|n'\rangle$ state in the right lead. We denote $\boldsymbol{t}_{\sigma'\sigma}$ as the scattering matrix of all orbital channels from the spin-σ state in the left lead to the spin-σ' state in the right lead, whose dimension is determined by the total number of the conducting channels. In particular, $\boldsymbol{t}_{\sigma'\sigma}$ can be calculated from the Green's function formalism [40,41].

We focus on calculating the physical quantities that are important to characterizing spin transport, such as the spin-resolved transmission coefficient $T^{\sigma'\sigma}$, the spin polarization vector $\boldsymbol{P}^{\sigma}$, and the spin-resolved shot noise characterized by the Fano factor F. For simplicity, throughout the work we assume polarized injection with $\sigma=\uparrow$ at the contact with the left lead. Omitting the index σ and writing $\boldsymbol{P}^{\sigma}$ as $\boldsymbol{P}$ would thus lead to no confusion.

Spin-resolved transmission. With the outgoing state Eq. (3), we obtain the spin-resolved transmission coefficients as

$$T^{\sigma'\sigma}=\text{Tr}(\boldsymbol{t}_{\sigma'\sigma}\boldsymbol{t}^{\dagger}_{\sigma'\sigma}),\quad \sigma,\sigma'=\uparrow,\downarrow, \tag{4}$$

which describes the transmission of the spin-σ incoming wave through the cavity and being detected as the spin-σ' wave in the right lead. At low temperature, the spin-resolved conductance can be obtained via the Landauer-Büttiker formula [8]: $G^{\sigma'\sigma}=(2e^2/h)T^{\sigma'\sigma}$. The total transmission is the sum of transmission for both spins, i.e., $T=\sum_{\sigma'}T^{\sigma'\sigma}$.

Spin polarization vector. The spin polarization vector is defined as [40,41,43] the average of the Pauli operator $\boldsymbol{P}=\langle\hat{\boldsymbol{\sigma}}\rangle$. It is necessary to normalize the outgoing state with the normalization constant

$$\sqrt{\sum_{\sigma'}\text{Tr}(\boldsymbol{t}_{\sigma'\sigma}\boldsymbol{t}^{\dagger}_{\sigma'\sigma})}=\sqrt{\text{Tr}(\boldsymbol{t}_{\uparrow\sigma}\boldsymbol{t}^{\dagger}_{\uparrow\sigma})+\text{Tr}(\boldsymbol{t}_{\downarrow\sigma}\boldsymbol{t}^{\dagger}_{\downarrow\sigma})}.$$

We have

$$|\text{out}\rangle=\sum_{n',\sigma'}\frac{\boldsymbol{t}_{n'n,\sigma'\sigma}}{\sqrt{\sum_{\sigma'}\text{Tr}(\boldsymbol{t}_{\sigma'\sigma}\boldsymbol{t}^{\dagger}_{\sigma'\sigma})}}|n'\rangle\otimes|\sigma'\rangle. \tag{5}$$

The spin polarization vector taking into account all injecting channels is given by [40]

$$\boldsymbol{P}=\sum_{n}\langle\text{out}|\hat{\boldsymbol{\sigma}}|\text{out}\rangle=\frac{\sum_{\sigma'\sigma''}\text{Tr}(\boldsymbol{t}_{\sigma'\sigma}\boldsymbol{t}^{\dagger}_{\sigma''\sigma})\langle\sigma'|\hat{\boldsymbol{\sigma}}|\sigma''\rangle}{\text{Tr}(\boldsymbol{t}_{\uparrow\sigma}\boldsymbol{t}^{\dagger}_{\uparrow\sigma})+\text{Tr}(\boldsymbol{t}_{\downarrow\sigma}\boldsymbol{t}^{\dagger}_{\downarrow\sigma})}. \tag{6}$$

This result has the same form as that in Ref. [40], which was obtained through the spin density matrix. Note that $|\boldsymbol{P}|=1$ indicates a pure state, while $|\boldsymbol{P}|<1$ specifies a mixed state as a result of loss of spin coherence into the environment.

Since the spin for the incoming state is assumed to be $\sigma=\uparrow$, the three components of $\boldsymbol{P}$ can be obtained from Eq. (6) as

$$P_x=\frac{2\,\text{Re}[\text{Tr}(\boldsymbol{t}_{\downarrow\uparrow}\boldsymbol{t}^{\dagger}_{\uparrow\uparrow})]}{\text{Tr}(\boldsymbol{t}_{\uparrow\uparrow}\boldsymbol{t}^{\dagger}_{\uparrow\uparrow})+\text{Tr}(\boldsymbol{t}_{\downarrow\uparrow}\boldsymbol{t}^{\dagger}_{\downarrow\uparrow})}, \tag{7a}$$

$$P_y=\frac{2\,\text{Im}[\text{Tr}(\boldsymbol{t}_{\downarrow\uparrow}\boldsymbol{t}^{\dagger}_{\uparrow\uparrow})]}{\text{Tr}(\boldsymbol{t}_{\uparrow\uparrow}\boldsymbol{t}^{\dagger}_{\uparrow\uparrow})+\text{Tr}(\boldsymbol{t}_{\downarrow\uparrow}\boldsymbol{t}^{\dagger}_{\downarrow\uparrow})}, \tag{7b}$$

$$P_z=\frac{\text{Tr}(\boldsymbol{t}_{\uparrow\uparrow}\boldsymbol{t}^{\dagger}_{\uparrow\uparrow})-\text{Tr}(\boldsymbol{t}_{\downarrow\uparrow}\boldsymbol{t}^{\dagger}_{\downarrow\uparrow})}{\text{Tr}(\boldsymbol{t}_{\uparrow\uparrow}\boldsymbol{t}^{\dagger}_{\uparrow\uparrow})+\text{Tr}(\boldsymbol{t}_{\downarrow\uparrow}\boldsymbol{t}^{\dagger}_{\downarrow\uparrow})}. \tag{7c}$$

For the incoming wave, we have $P_z=1$. Our goal is to assess the value of P_z after scattering from the cavity.

Spin-resolved shot noise. Quantum transmission is related with the current through the system. The shot noise characterizes the current's fluctuation-correlation function, which can be an indicator of the randomness of the system [45–48] and can be measured in experiments with apparatus as described in Ref. [48]. At low temperatures and on the mesoscopic scale, the electron's mean free path can be larger than the system size, making the conductor phase coherent. The origin and the meaning of shot noise for phase-coherent transport system has been explained in Refs. [45–48]. Specifically, in general, the quantum states are occupied by particles in a probabilistic sense as characterized, e.g., by the transmission probability (coefficient) from the incoming to the outgoing channels [49]. Shot noise originates from the fluctuations of the particles. When spin is not taken into consideration, the scattering theory of quantum transport can be used to obtain [45–48] the following formula for the shot noise power in terms of the transmission eigenvalues:

$$S=\frac{4e^3V}{h}\sum_{n}T_n(1-T_n),$$

where T_n are the eigenvalues of the transmission matrix $\mathbf{t}\mathbf{t}^{\dagger}$ and V is the applied voltage in the longitudinal (transport) direction. When spin is taken into account, shot noise for spin-resolved transport process can be obtained [41] similar to that of the spin polarization vector for the setup $\sigma=\uparrow$. More specifically, the four components of shot noise are

$$S^{\uparrow\uparrow}=\frac{2e^3V}{h}[\text{Tr}(\boldsymbol{t}_{\uparrow\uparrow}\boldsymbol{t}^{\dagger}_{\uparrow\uparrow})+\text{Tr}(\boldsymbol{t}_{\uparrow\uparrow}\boldsymbol{t}^{\dagger}_{\uparrow\uparrow}\boldsymbol{t}_{\uparrow\uparrow}\boldsymbol{t}^{\dagger}_{\uparrow\uparrow})], \tag{8a}$$

$$S^{\downarrow\downarrow}=\frac{2e^3V}{h}[\text{Tr}(\boldsymbol{t}_{\downarrow\uparrow}\boldsymbol{t}^{\dagger}_{\downarrow\uparrow})+\text{Tr}(\boldsymbol{t}_{\downarrow\uparrow}\boldsymbol{t}^{\dagger}_{\downarrow\uparrow}\boldsymbol{t}_{\downarrow\uparrow}\boldsymbol{t}^{\dagger}_{\downarrow\uparrow})], \tag{8b}$$

$$S^{\uparrow\downarrow}=-\frac{2e^3V}{h}\text{Tr}(\boldsymbol{t}_{\downarrow\uparrow}\boldsymbol{t}^{\dagger}_{\uparrow\uparrow}\boldsymbol{t}_{\uparrow\uparrow}\boldsymbol{t}^{\dagger}_{\downarrow\uparrow}), \tag{8c}$$

$$S^{\downarrow\uparrow}=-\frac{2e^3V}{h}\text{Tr}(\boldsymbol{t}_{\uparrow\uparrow}\boldsymbol{t}^{\dagger}_{\downarrow\uparrow}\boldsymbol{t}_{\downarrow\uparrow}\boldsymbol{t}^{\dagger}_{\uparrow\uparrow}). \tag{8d}$$

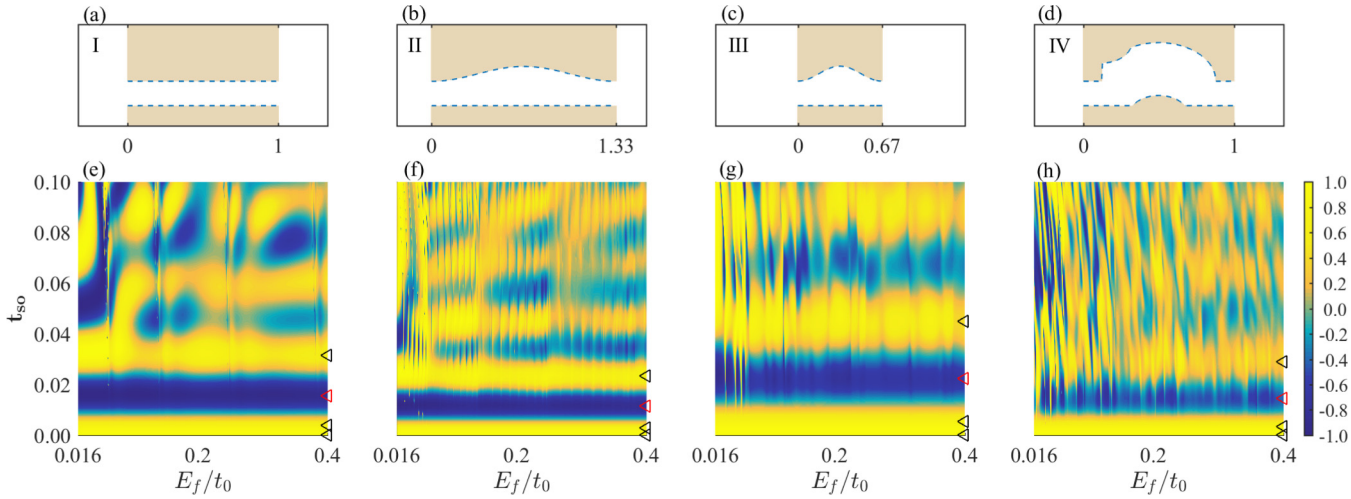

FIG. 2. Four cavities investigated in this paper and their spin polarization. [(a)–(d)] Cavities I to IV in the order of an increasing degree of classical chaos, respectively. All structures have the same width of 0.24 μm and, for a given Fermi energy, the leads permit the same number of transmitting modes. (a) A ribbon with integrable classical dynamics, where the length of the SOC region is 1 μm. (b) A cosine billiard with mixed dynamics of length $L = 1.33$ μm. The upper boundary is given by [21] $y = W + (M/2)[1 - \cos(2\pi x/L)]$ with $M/L = 0.11$ and $W/L = 0.18$. (c) A cosine billiard with chaotic dynamics for $L = 0.67$ μm, $M/L = 0.22$, and $W/L = 0.36$. (d) A chaotic cavity [44] with its upper boundary being made up of an arc of radius $R = 0.38$ μm and another arc of radius $r = 0.2$ μm. The lower boundary is a section of arc of radius $r = 0.2$ μm. The length of the cavity is 1 μm. [(e)–(h)] Contour plots of P_z in the parameter plane of Fermi energy E_f and SOC strength t_{so} (both in units of t_0, the hopping energy between neighboring lattice sites). The triangles mark the positions of the t_{so} such that $L_{so} = \pi/(2t_{so}) = \infty, 4L, L, L/2$, which are investigated further in Fig. 3.

The spin-resolved current induced by the incoming spin up electrons is [41]

$$I^{\sigma} = \frac{2e^2V}{h}\mathrm{Tr}(\boldsymbol{t}_{\sigma\uparrow}\boldsymbol{t}^{\dagger}_{\sigma\uparrow}), \quad \sigma = \uparrow, \downarrow . \tag{9}$$

The Fano factor, by its definition $F = S/(2eI)$, can also be obtained in a spin-resolved manner as

$$F^{\uparrow\to\uparrow} = \frac{S^{\uparrow\uparrow}}{2eI^{\uparrow}}, \tag{10a}$$

$$F^{\uparrow\to\downarrow} = \frac{S^{\downarrow\downarrow}}{2eI^{\downarrow}}, \tag{10b}$$

$$F^{\uparrow\to\uparrow\downarrow} = \frac{S}{2eI}, \tag{10c}$$

where $I = I^{\uparrow} + I^{\downarrow}$, and $S = S^{\uparrow\uparrow} + S^{\uparrow\downarrow} + S^{\downarrow\uparrow} + S^{\downarrow\downarrow}$. For convenience, we denote $F^{\uparrow\to\uparrow\downarrow}$ as F. The value of the Fano factor lies in the range [0, 1] [41], where a larger value of F indicates a stronger degree of randomness in channel mixing [49–51]. For completely stochastic motion, we have $F = 1$, and the corresponding shot noise of this case is Poisson [46,47]. For $F \to 0$, the electron motions are deterministic [48–53]. In general, the value of the Fano factor is an indicator of the quantum randomness in the current that coincides with the degree of classical chaos of the system [49–51].

III. RESULTS

We employ the Usuki recursive scattering matrix technique [37] to calculate the three characterizing quantities described in Sec. II. The characteristic length scale associated with spin transport is the distance required for spin to flip in the semiclassical regime, which is the so-called spin-orbit length [40,41,54] defined as

$$L_{so} = \pi\hbar^2/(2m^*\alpha) = \pi a t_0/(2t_{so}),$$

where a is the lattice constant and $t_0 = \hbar^2/(2m^*a^2)$ is the hopping energy between two neighboring sites. In the units of $a = \hbar = 2m^* = 1$, we have $t_0 = 1$, so $L_{so} = \pi/(2t_{so})$.

Figures 2(a)–2(d) show the four cavities that we study, which are denoted as cavities I–IV, respectively. The classical dynamics for cavity I and II are integrable and mixed, respectively, while those of cavities III and IV are fully chaotic. It has been noted that with spin-orbit interactions only circular billiard is integrable [55,56], but in our case, integrable or chaos are referred to the corresponding classical dynamics only. Since it is assumed that the orbital motion is not affected by spin, the orbital motion is purely determined by the classical trajectories [33–36], and the cavity shape determines the classical integrability of the system. For the purpose of comparison, the leads attached to the cavities in all cases have the same width so that, for a given energy, there are an equal number of transmitting modes in the lead. Figures 2(e)–2(h) present the contour plots of spin polarization P_z in the parameter plane of Fermi energy E_f and spin-orbit coupling strength t_{so}, for the cavities in Figs. 2(a)–2(d), respectively. For relatively small values of t_{so}, P_z varies periodically with t_{so}. However, as the value of t_{so} becomes larger, the periodic behavior disappears due to the phenomenon of spin subband mixing [57]. Our computations reveal that transmission and shot noise exhibit a similar pattern as the value of t_{so} is increased from zero, which has also been observed in previous works [57,58]. We note that, as the classical dynamics become increasingly chaotic [Fig. 2(e) to Fig. 2(h)], the periodic pattern of P_z versus t_{so} becomes progressively degraded. Another feature is that, as E_f is increased, P_z exhibits vertical line

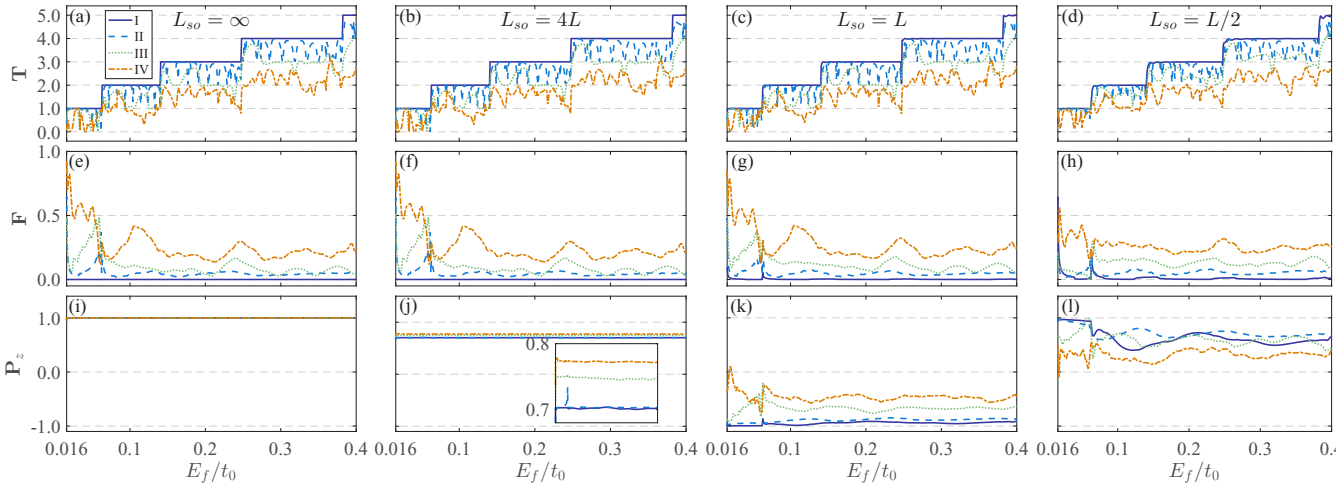

FIG. 3. Characterization of spin transport through the four different types of cavities. Total transmission $T = T^{\uparrow\uparrow} + T^{\downarrow\uparrow}$ (upper row), charge Fano factor $F \equiv F^{\uparrow\to\uparrow\downarrow}$ [Eq. (10c)] for the total spin-resolved current (middle row), and the spin polarization P_z (bottom row) vs the normalized Fermi energy. The four columns from left to right correspond to $L_{\rm so} = \infty$, $4L$, L, $L/2$, respectively. The notions I–IV indicate the four cavities in Fig. 2. For F and P_z, a sliding window average is used with the window size $\Delta = 0.0464t_0$. For $E_f - 0.016t_0 < \Delta/2$, the average is over the interval $[0.016t_0, 2E_f - 0.016t_0]$.

patterns, which can be seen clearly from Fig. 2(e). This is due to the abrupt changes in the number of transmitting modes as E_f is increased, i.e., from one to two, to three, and to four. There are many more vertical lines in (f) due to the localized states about the stable periodic orbits in cavity II with mixed dynamics in the classical limit. The nearly vertical curves in Figs. 2(g) and 2(h) are also due to the localized states but, because of the absence of stable periodic orbits in a chaotic cavity, these states are much weaker than those in the mixed cavity, resulting in much smoother variations of P_z with E_f.

It is insightful to examine the details of the dependence of the total transmission, the Fano factor of the total current, and the spin polarization P_z on the Fermi energy E_f for some specific values of $t_{\rm so}$, as marked by the four triangles in each of Figs. 2(e)–2(h), corresponding to $L_{\rm so} = \pi/(2t_{\rm so}) = \infty$, $4L$, L, $L/2$, where there is absence of spin precession, $\pi/4$ precession for the ribbon, up to down spin flip, up to down and then back to up spin flip, respectively. The results for the four cases are shown in Fig. 3.

For the ribbon, the total transmission is a step function versus the Fermi energy, corresponding to the number of allowed transmitting modes, where the first transmitting mode emerges at the Fermi energy $0.016t_0$, below which there are no transmitting modes and the total transmission is zero. As the spin-orbit coupling becomes stronger [Figs. 3(c) and 3(d)], the total transmission exhibits small oscillations after jumps, which is similar to what happens when a magnetic field is present. As the cavity becomes increasingly chaotic in the classical limit (from I to IV), random scattering becomes more severe, leading to degraded transmission. The four curves for the transmission in Figs. 3(a)–3(d) from top to down are for cavities I to IV, respectively. For mixed classical dynamics (cavity II), due to the recurrence of the strongly localized states about the stable periodic orbits, the transmission exhibits repeated oscillations as E_f is varied. For the chaotic cavities (III and IV), the transmission becomes irregular.

Figures 3(e)–3(h) show that, as the cavity becomes more chaotic, the Fano factor of the total current takes on larger values, indicating a stronger degree of randomness associated with channel mixing of the current [51,53]. The Fano factor is thus a quantity capable of revealing faithful quantum manifestations of classical chaos [49–53]. We find that these results are insensitive to the specific values of $t_{\rm so}$ or $L_{\rm so}$, as the qualitative behaviors are essentially the same for different $t_{\rm so}$ values.

Figures 3(i)–3(l) show the spin polarization P_z versus the Fermi energy. For $L_{\rm so} = \infty$ or $t_{\rm so} = 0$ [Fig. 3(i)], there is no change in spin, leading to $P_z = 1$ (independent of the Fermi energy) for all cavities. For $L_{\rm so} = 4L$ [Fig. 3(j)], P_z decreases slightly. From the magnifying inset, we see a more dramatic decrease in the value of P_z for the ribbon than that for the chaotic cavities, indicating that classical chaos helps to preserve the spin polarization. As the spin-orbit coupling is strengthened further, e.g., for $L_{\rm so} = L$ [Fig. 3(k)], spin flips begin to occur. For the ribbon, P_z can reach the value of -1. However, as the cavity becomes more chaotic, P_z approaches zero, demonstrating the destructive effects of chaos on spin polarization. For $L_{\rm so} = L/2$ [Fig. 3(l)], spin flips to the up state again, i.e., $P_z > 0$. In this case, P_z exhibits a decreasing trend from ribbon to mixed and then to chaotic cavities, signifying again the destructive role of chaos in spin polarization.

To characterize the effects of chaos on spin polarization more quantitatively, we average P_z in the energy range with certain number of transmitting modes. Figures 4(a)–4(d) show the average spin polarization $\langle P_z\rangle_{E_f}$ versus $t_{\rm so}$ for the energy range with one to four transmitting modes, respectively. In all panels, $\langle P_z\rangle_{E_f}$ oscillates periodically with $t_{\rm so}$ but with a decreasing amplitude, which can be attributed to channel mixing in the regime of strong spin-orbit coupling. Figures 4(a)–4(d) reveal two distinct regimes of $t_{\rm so}$: $t_{\rm so}/\tilde{t}_{\rm so} \leqslant 1/2$ ($L_{\rm so} \geqslant 2L$) and $t_{\rm so}/\tilde{t}_{\rm so} \geqslant 1$ ($L_{\rm so} \leqslant L$). For $t_{\rm so}/\tilde{t}_{\rm so} < 1/2$, $\langle P_z\rangle_{E_f}$ decreases from unity and the fastest decay occurs for the ribbon (cavity

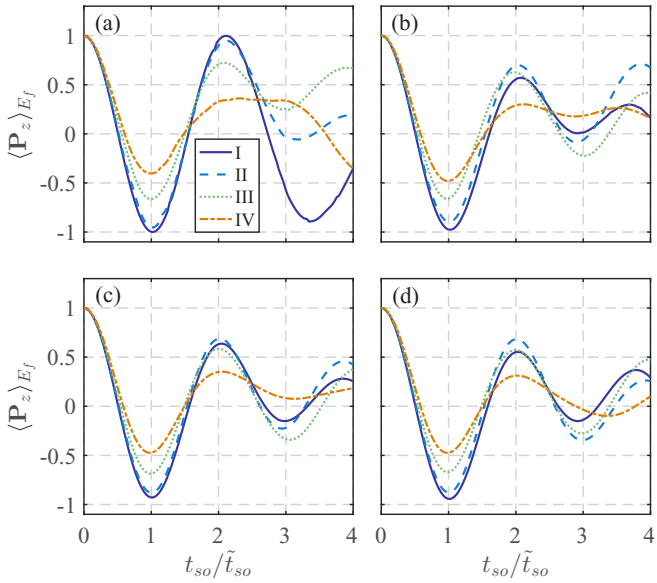

FIG. 4. Averaged spin polarization over the Fermi energy vs the spin-orbit coupling strength. [(a)–(d)] Averaged polarization $\langle P_z\rangle_{E_f}$ versus $t_{\rm so}$ for four different ranges of energy averaging: [0.016, 0.0624], [0.0632, 0.140], [0.1408, 0.2472], [0.248, 0.3816], respectively, corresponding to one to four transmission modes. The spin-orbit coupling strength $t_{\rm so}$ is normalized by $\tilde{t}_{\rm so}$, the strength value that flips the electron spin from up to down as it travels from the left to the right lead through the cavity. The $\tilde{t}_{\rm so}$ values are marked by the third triangles (red) from the bottom in Fig. 2 for different cavities.

I). As the cavity becomes increasingly chaotic, the decay of $\langle P_z\rangle_{E_f}$ becomes slower, and the slowest decay occurs for cavity IV. For $t_{\rm so}/\tilde{t}_{\rm so} = 1/2$, we have $\langle P_z\rangle_{E_f} = 0$ for the ribbon, while the value of $\langle P_z\rangle_{E_f}$ is still finite for the chaotic cavities. We can conclude that, in this regime (e.g., $L_{\rm so} = 4L$ or $t_{\rm so}/\tilde{t}_{\rm so} = 1/4$ as in Fig. 3), chaos is beneficial to preserving spin polarization. Beyond this regime, the value of $\langle P_z\rangle_{E_f}$ gets close to -1 for the ribbon as $t_{\rm so}/\tilde{t}_{\rm so}$ approaches one (the case $L_{\rm so} = L$). For the other cavities, although $\langle P_z\rangle_{E_f}$ attains a minimum value, the value of $|\langle P_z\rangle_{E_f}|$ is typically smaller than one and closer to zero for a more chaotic cavity. For example, for cavity IV, the value of $\langle P_z\rangle_{E_f}$ approaches the value of approximately -0.5. In these cases, chaos is detrimental to spin polarization. This feature persists for $t_{\rm so}/\tilde{t}_{\rm so} \geqslant 1$, e.g., $L_{\rm so} = L/2$ (corresponding to $t_{\rm so}/\tilde{t}_{\rm so} = 2$) in Fig. 3.

IV. SEMICLASSICAL THEORY

Our full quantum computations have revealed that, for polarized injection, depending on the relative scale of the characteristic spin-orbit interaction length, classical chaos can either preserve or destroy quantum spin polarization. Here we present a semiclassical theory to explain these results. The starting point is to rewrite the Hamiltonian in (1) as [1,59]

$$\hat{\mathcal{H}} = \frac{\hat{\boldsymbol{p}}^2}{2m^*}\sigma_0 + \frac{\hbar}{2}\hat{\boldsymbol{\sigma}}\cdot\hat{\boldsymbol{\Omega}}, \tag{11}$$

where $\hat{\boldsymbol{\Omega}} = -(2/\hbar^2)\boldsymbol{\alpha}\times\hat{\boldsymbol{p}}$. The Hamiltonian is valid for electron inside the cavity, subject to Rashba spin-orbit interaction. The equation of time evolution of the spin polarization vector $\boldsymbol{P} = \langle\hat{\boldsymbol{\sigma}}\rangle$ is given by [1,59]

$$\frac{d}{dt}\langle\hat{\boldsymbol{\sigma}}\rangle = \frac{1}{i\hbar}\langle[\hat{\boldsymbol{\sigma}},\hat{\mathcal{H}}]\rangle = \langle\hat{\boldsymbol{\Omega}}\times\hat{\boldsymbol{\sigma}}\rangle. \tag{12}$$

For this system, the two observables $\{\hat{\boldsymbol{p}},\hat{\boldsymbol{\sigma}}\}$ form a complete set of variables. The quantum state $|\psi\rangle$ of the system can then be chosen as the eigenstate of both $\hat{\boldsymbol{p}}$ and $\hat{\boldsymbol{\sigma}}$. We thus have $\langle\hat{\boldsymbol{p}}\rangle = \boldsymbol{p}$, $\langle\hat{\boldsymbol{\Omega}}\rangle = \boldsymbol{\Omega} = -(2/\hbar^2)\boldsymbol{\alpha}\times\boldsymbol{p}$ and $\langle\hat{\boldsymbol{\sigma}}\rangle = \boldsymbol{P}$. With these expressions, Eq. (12) can be further simplified as [1,59]

$$\frac{d}{dt}\boldsymbol{P} = \boldsymbol{\Omega}\times\boldsymbol{P}, \tag{13}$$

which describes the rotational motion of the polarization vector $\boldsymbol{P}$ about $\boldsymbol{\Omega}$, with $|\boldsymbol{\Omega}|$ being the angular velocity of $\boldsymbol{P}$.

Semiclassically, an electron moves freely in the cavity and reflects at the boundary, so the trajectory consists of straight line segments. For each segment, $\boldsymbol{\Omega}$ is a constant, for which Eq. (13) can be solved analytically. In particular, let $\boldsymbol{P}$ and $\boldsymbol{P}'$ be the polarization vectors at the beginning and end of a straight trajectory segment, respectively. The two vectors are connected through a rotation matrix as

$$\boldsymbol{P}' = \mathcal{R}(\gamma,\varphi)\boldsymbol{P}, \tag{14}$$

where the matrix is given by

$$\mathcal{R}(\gamma,\varphi) = \begin{pmatrix} \cos\varphi + (1-\cos\varphi)\sin^2\gamma & -\sin\gamma\cos\gamma(1-\cos\varphi) & -\cos\gamma\sin\varphi \\ -\sin\gamma\cos\gamma(1-\cos\varphi) & \cos\varphi + (1-\cos\varphi)\cos^2\gamma & -\sin\gamma\sin\varphi \\ \cos\gamma\sin\varphi & \sin\gamma\sin\varphi & \cos\varphi \end{pmatrix}.$$

Here, φ is the rotated angle. The axis of rotation is determined by γ: for momentum $\boldsymbol{p} = p(\cos\gamma,\sin\gamma,0)$, we have $\boldsymbol{\Omega} = -(2/\hbar^2)\boldsymbol{\alpha}\times\boldsymbol{p} = [(2\alpha p)/\hbar^2]\boldsymbol{n}$, where $\boldsymbol{\alpha} = -[\hbar/(2m^*c)^2]\boldsymbol{E}_{\rm Rashba}$ is the Rashba spin-orbit coupling strength pointing to the z direction, $\boldsymbol{n}$ is a unit vector perpendicular to the plane spanned by $\boldsymbol{\alpha}$ and $\boldsymbol{p}$, thus the rotation axis is given by $\boldsymbol{n} = (\sin\gamma,-\cos\gamma,0)$. Since

$$d\boldsymbol{\varphi} = \boldsymbol{\Omega}dt = -\frac{2m^*}{\hbar^2}\boldsymbol{\alpha}\times d\boldsymbol{r}, \tag{15}$$

and because α is a constant, $d\boldsymbol{r}$ is along the line segment. We thus have $\varphi = (2m^*\alpha/\hbar^2)s$, where s is the distance that the electron travels through [60]. For $s = L_{\rm so}$, we have $\varphi = \pi$. After n reflections at the boundary, the final polarization vector is related to the initial one by $\boldsymbol{P}_f = \mathcal{R}_n\cdot\cdots\cdot\mathcal{R}_1\cdot\boldsymbol{P}_i$.

For different types of classical dynamics, the trajectories can be characteristically distinct. For example, for the ribbon, the trajectory segments have two directions only and the trajectory takes these directions alternatively during

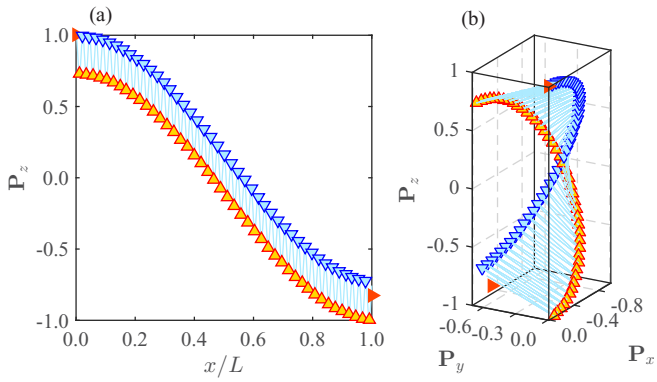

FIG. 5. Spin polarization and evolution of polarization vector for the integrable cavity. For the ribbon (cavity I), (a) P_z vs x, for spin-orbit coupling strength $L_{so} = L$. Symbols are numerical results from Eq. (14), while the light blue oscillatory curve is from theory [Eq. (16)]. (b) A trajectory of the spin polarization vector in the $\boldsymbol{P}$ space, where up and down triangles are for reflections from the upper and lower boundary, respectively.

evolution: $\gamma_0, -\gamma_0, \gamma_0, \ldots$, where γ_0 is the initial angle with respect to x axis. The rotated angle for each line segment is $\varphi_0 = 2m^*\alpha M/[\hbar^2 \sin(\gamma_0)]$. Denoting $\mathcal{R}_0 = \mathcal{R}(\gamma_0, \varphi_0)$ and $\mathcal{R}_1 = \mathcal{R}(-\gamma_0, \varphi_0)$, we have $\boldsymbol{P}_f = \cdots \cdot \mathcal{R}_1 \cdot \mathcal{R}_0 \cdot \mathcal{R}_1 \cdot \mathcal{R}_0 \cdot \boldsymbol{P}_i$. We thus have the following approximate expressions for the spin polarization vector as it propagates along the x axis:

$$P_x(x) = -\cos\left(\frac{\pi M}{2L_{so}}\right)\sin\left[(1+\omega_1)\frac{\pi}{L_{so}}x\right], \tag{16a}$$

$$P_y(x) = -\sin\left(\frac{\pi M}{2L_{so}}\right)\cos\left(\frac{\pi M}{2L_{so}}\right)\left\{1-\cos\left[(1+\omega_1)\frac{\pi}{L_{so}}x\right] \times \cos\left[(1+\omega_2)\frac{\pi}{M\cot\gamma}x\right]\right\}, \tag{16b}$$

$$P_z(x) = \cos^2\left(\frac{\pi M}{2L_{so}}\right)\cos\left[(1+\omega_1)\frac{\pi}{L_{so}}x\right] + \sin^2\left(\frac{\pi M}{2L_{so}}\right) \times \cos\left[(1+\omega_2)\frac{\pi}{M\cot\gamma}x\right]. \tag{16c}$$

where the values of ω_1 and ω_2 depend on the parameters of the system. Figures 5(a) and 5(b) show, for $\omega_1 = -2.065M\cot\gamma_0/L$, and $\omega_2 = -0.001\omega_1$, P_z versus x and the evolution of the whole spin polarization vector, respectively. The initial spin polarization is $\boldsymbol{P}_i = [0, 0, 1]^T$. The symbols are the numerically calculated values of spin polarization from Eq. (14), while the curves represent the theoretical prediction from Eq. (16). There is good agreement between theory and numerics. Different choices of the parameters M and L will lead to different values of ω_1 and ω_2, but Eq. (16) still holds.

For mixed or chaotic classical dynamics, due to the variations of the rotating axis and angle, analytic expressions similar to Eq. (16) cannot be obtained. Nevertheless, it is feasible to calculate the classical phase space and examine how a typical trajectory behaves. In particular, we can trace the trajectory and calculate the corresponding spin polarization

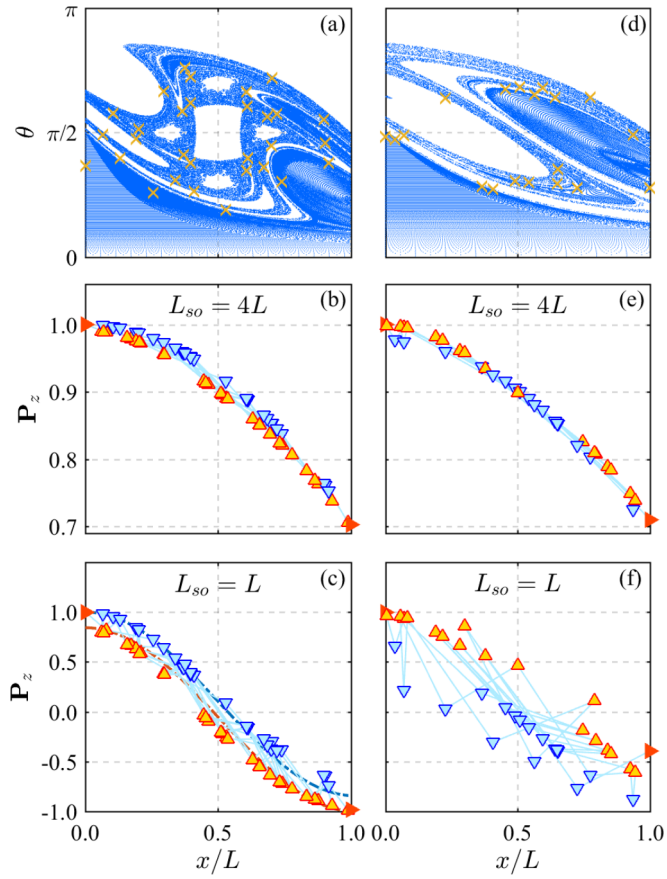

FIG. 6. Spin polarization and evolution of polarization vector for cavities with mixed and chaotic dynamics. [(a) and (d)] Phase space trajectories, i.e., the reflection angle versus the position of reflection at the lower boundary, for the cosine cavity with mixed (cavity II) and chaotic dynamics (cavity III), respectively. Only trajectories starting from the left lead are considered. The crosses are for a typical trajectory [61]. A dominant KAM island at $(x, \theta) = (0.5, \pi/2)$ is present in (a). [(b) and (e)] P_z vs x for the trajectories shown in [(a) and (d)], respectively. The spin-orbit coupling strength is such that $L_{so} = 4L$. (c,f) P_z versus x for the same trajectories but with $L_{so} = L$. The two curves in (c) are the envelope lines similar to that in Fig. 5(a). Up and down triangles are for trajectory's reflecting from the upper and lower boundary, respectively. The two solid red right triangles mark the values of the incoming and outgoing P_z at $x = 0$ and $x = L$, respectively.

vector to gain insights into their relation, so as to assess the influence of the classical dynamics on the evolution of the spin polarization vector in terms of the distinct behaviors of the trajectories. Representative results are shown in Fig. 6. The left column is for the mixed case (cavity II), where a dominant KAM island is apparent in the phase space [Fig. 6(a)]. A typical trajectory is located around the KAM island, i.e., the trajectory stays close to the periodic orbit for a substantially long time due to the stickiness effect of the KAM island [62–66]. As a result, the reflection angle and the segment length between two successive reflections vary in an ordered manner, similar to the behaviors in an integrable cavity. Since the reflection angle and the segment length are uniquely determined by the axis angle γ and the angle of rotation φ

in Eq. (14), the corresponding spin polarization P_z varies in a way similar to that for the ribbon, as shown in Figs. 6(b) and 6(c), in spite of the many bounces back and forth in the x direction. For the chaotic cavity (III), there are no KAM tori and the phase space is filled with chaotic sea, as shown in Fig. 6(d). A typical trajectory bounces randomly with large variations in the reflection angle and the segment length, leading to drastic changes in the rotating axis.

For weak spin-orbit coupling, e.g., $L_{so} = 4L$, the rotating angle φ is small. For the chaotic case, due to the stochastic variations in the rotating axis angle γ, the evolution of the spin polarization vector mimics a random walk about its starting point, leading to an appreciable value of P_z higher than the values for the integrable or mixed cavities, as shown in Figs. 6(b) and 6(e). For strong spin-orbit coupling, e.g., $L_{so} = L$, after the electron passes through the Rashba region, the value of P_z is close to -1 for the integrable and mixed cavities [Figs. 5(a) and 6(c), respectively]. However, for the chaotic cavity, P_z varies drastically, as shown in Fig. 6(f), leading to a deteriorated output spin polarization on average.

V. DISCUSSION AND CONCLUSION

Fundamentally, spin is a relativistic quantum degree of freedom, for which a classical correspondence does not exist. Nonetheless, spin-orbit interactions provide an avenue through which classical dynamics are able to manifest themselves in the characteristics and evolution of spin. In particular, for billiards with Rashba spin-orbit interactions, previous works have investigated conductance fluctuations [67,68], statistical properties of wave functions [69,70], the effects to weak localization and weak antilocalization [71], and other characteristics in the general context of quantum chaos [72–74]. In a general sense, to study the effects of distinct types of classical dynamics including chaos on spin belongs to the field of relativistic quantum chaos [75,76]. Concerning only the impact of classical chaos on spin behaviors, there have been previous works on closed systems but with seemingly contradicting conclusions: situations were identified where chaos preserves or enhances spin polarization [35], but there are also circumstances under which chaos plays the opposite role of deteriorating the polarization [36].

In this paper, we present results from a systematic study of the effects of classical chaos on spin transport. We focus on spin transport in 2D quantum dot systems with Rashba spin-orbit interaction and investigate systematically the effects of classically integrable, mixed, and chaotic dynamics on spin polarization. For a given dot structure with a specific class of classical dynamics, we assume that spin polarized electrons are injected into the system and carry out full quantum computations to obtain an exact picture of how the spin polarization evolves during the transport through the dot. To gain insights, we also develop a semiclassical theory to obtain a physical understanding of the phenomena revealed by the quantum calculations. This should be contrast to previous works that were based mainly on the semiclassical approach [35,36]. We find that classical chaos has a clear signature in the Fano factor for spin-resolved quantum transport. Strikingly, in the weak spin-orbit coupling regime where the characteristic interaction length is relatively large, classical chaos is beneficial to preserving spin polarization, but in the strong coupling regime, chaos can suppress or even destroy the polarization.

Conceptually, in the weak coupling regime, the dynamics of spin polarization are described by those of a damped oscillator. For classically integrable dynamics, the oscillations are regular with small damping effects. As the classical dynamics become increasingly chaotic, damping becomes significant. For any oscillation period, in the first quarter, spin polarization for the integrable dot decreases rapidly to zero, while that for the chaotic system decreases much more slowly, giving rise to the counterintuitive phenomenon of chaos-assisted spin polarization preservation. In the strong spin-orbit coupling regime with characteristic length smaller than the size of the interacting region, chaos is detrimental to spin polarization. An implication is that, for a given strength of spin-orbit interaction, chaos in a relatively small quantum dot system can preserve spin polarization, but the opposite occurs in a larger system.

Our computations and analysis provide a natural understanding of the seemingly contradicting results reported previously in the literature. For example, in Ref. [35], the parameters are such that the characteristic spin-orbit length is much larger than the scale of the quantum dot (antidot). Semiclassically, the angle of spin rotation per scattering event or collision is small. From the point of view of ensemble average, chaos can suppress the overall spin drift and help maintain the spin polarization. The phenomenon reported in Ref. [36] has a similar origin. However, when the characteristic spin-orbit length is comparable to or even smaller than the system size, spin polarization depends primarily on the classical periodic orbits [36]. For a chaotic dot system, the periodic orbits are unstable, which accelerates relaxation of spin polarization.

We have also examined graphene quantum dots with the same cavity structures and found essentially the same results. Our results have broad applications in developing devices where robust maintenance of spin polarization is required. This is because chaos plays the same role as disorder or edge roughness in an experimental setup to provide randomness in transport through quantum dots. In particular, as smaller systems are becoming increasingly experimentally accessible and are exploited for device applications, our results indicate that when the system is smaller than the characteristic spin-orbit length, disorders or edge roughness can be beneficial to maintaining spin polarization.

ACKNOWLEDGMENTS

We would like to thank Prof. B. Dietz for illuminating discussions. This work is supported by NNSF of China under Grant Nos. 11422541 and 11775101, and by the Fundamental Research Funds for the Central Universities under Grant No. lzujbky-2016-k05. The work at Arizona State University is supported by the Vannevar Bush Faculty Fellowship program sponsored by the Basic Research Office of the Assistant Secretary of Defense for Research and Engineering and funded by the Office of Naval Research through Grant No. N00014-16-1-2828.

[1] I. Žutić, J. Fabian, and S. D. Sarma, Rev. Mod. Phys. **76**, 323 (2004).
[2] A. Fert, Rev. Mod. Phys. **80**, 1517 (2008).
[3] V. Baltz, A. Manchon, M. Tsoi, T. Moriyama, T. Ono, and Y. Tserkovnyak, Rev. Mod. Phys. **90**, 015005 (2018).
[4] B. Azzerboni, G. Asti, L. Pareti, and M. Ghidini, *Magnetic Nanostructures in Modern Technology* (Springer, Netherlands, 2008).
[5] Y. B. Xu and S. M. Thompson, *Spintronic Materials and Technology* (CRC Press, Florida, 2010).
[6] Y. S. Gui, N. Mecking, X. Zhou, G. Williams, and C. M. Hu, Phys. Rev. Lett. **98**, 107602 (2007).
[7] M. Harder, Y. Gui, and C. M. Hu, Phys. Rep. **661**, 1 (2016).
[8] S. Datta, *Electronic Transport in Mesoscopic Systems* (Cambridge University Press, Cambridge, England, 1995).
[9] P. A. Lee and A. D. Stone, Phys. Rev. Lett. **55**, 1622 (1985).
[10] C. P. Umbach, S. Washburn, R. B. Laibowitz, and R. A. Webb, Phys. Rev. B **30**, 4048 (1984).
[11] R. A. Webb, S. Washburn, C. P. Umbach, and R. B. Laibowitz, Phys. Rev. Lett. **54**, 2696 (1985).
[12] A. D. Stone, Phys. Rev. Lett. **54**, 2692 (1985).
[13] R. A. Jalabert, H. U. Baranger, and A. D. Stone, Phys. Rev. Lett. **65**, 2442 (1990).
[14] H. J. Stöckmann, *Quantum Chaos: An Introduction* (Cambridge University Press, Cambridge, England, 1999).
[15] Y.-C. Lai and T. Tél, *Transient Chaos: Complex Dynamics on Finite-Time Scales* (Springer, New York, 2011).
[16] R. Ketzmerick, Phys. Rev. B **54**, 10841 (1996).
[17] A. S. Sachrajda, R. Ketzmerick, C. Gould, Y. Feng, P. J. Kelly, A. Delage, and Z. Wasilewski, Phys. Rev. Lett. **80**, 1948 (1998).
[18] B. Huckestein, R. Ketzmerick, and C. H. Lewenkopf, Phys. Rev. Lett. **84**, 5504 (2000).
[19] A. P. S. de Moura, Y.-C. Lai., R. Akis, J. P. Bird, and D. K. Ferry, Phys. Rev. Lett. **88**, 236804 (2002).
[20] D. Vasileska and S. M. Goodnick, *Nano-Electronic Devices: Semiclassical and Quantum Transport Modeling* (Springer Publishing Company, New York, 2011).
[21] R. Yang, L. Huang, Y.-C. Lai, and C. Grebogi, Europhys. Lett. **94**, 40004 (2011).
[22] R. Bao, L. Huang, Y.-C. Lai, and C. Grebogi, Phys. Rev. E **92**, 012918 (2015).
[23] R. Yang, L. Huang, Y.-C. Lai, and L. M. Pecora, Appl. Phys. Lett. **100**, 093105 (2012).
[24] R. Yang, L. Huang, Y.-C. Lai, C. Grebogi, and L. M. Pecora, Chaos **23**, 013125 (2013).
[25] E. I. Rashba, Sov. Phys. Solid State **2**, 1109 (1960).
[26] E. I. Rashba, Phys. Rev. **140**, A401 (1965).
[27] E. I. Rashba, Phys. Rev. B **62**, R16267 (2000).
[28] L. P. Gor'kov and E. I. Rashba, Phys. Rev. Lett. **87**, 037004 (2001).
[29] E. I. Rashba and A. L. Efros, Phys. Rev. Lett. **91**, 126405 (2003).
[30] T. Koga, J. Nitta, H. Takayanagi, and S. Datta, Phys. Rev. Lett. **88**, 126601 (2002).
[31] J. Schliemann, J. C. Egues, and D. Loss, Phys. Rev. Lett. **90**, 146801 (2003).
[32] F. Zhai and H. Q. Xu, Phys. Rev. Lett. **94**, 246601 (2005).
[33] G. B. Akguc and J. Gong, Phys. Rev. B **77**, 205302 (2008).
[34] L. Ying and Y.-C. Lai, Phys. Rev. B **93**, 085408 (2016).
[35] Y. V. Pershin and V. Privman, Phys. Rev. B **69**, 073310 (2004).
[36] C. H. Chang, A. G. Mal'shukov, and K. A. Chao, Phys. Rev. B **70**, 245309 (2004).
[37] T. Usuki, M. Saito, M. Takatsu, R. A. Kiehl, and N. Yokoyama, Phys. Rev. B **52**, 8244 (1995).
[38] R. Akis, D. K. Ferry, J. P. Bird, and D. Vasileska, Phys. Rev. B **60**, 2680 (1999).
[39] X. Xiao, Z. Chen, W. Nie, G. Zhou, and F. Li, J. Appl. Phys. **115**, 223709 (2014).
[40] B. K. Nikolić and S. Souma, Phys. Rev. B **71**, 195328 (2005).
[41] B. K. Nikolić and R. L. Dragomirova, Semicond. Sci. Tech. **24**, 064006 (2009).
[42] L. D. Landau and E. M. Lifshitz, *Quantum Mechanics (Non-relativistic Theory)*, 3rd ed. (World Publishing Company, New York, 2007).
[43] Y. T. Zhang, Z. F. Song, and Y. C. Li, Phys. Lett. A **373**, 144 (2008).
[44] H. U. Baranger and P. A. Mello, Phys. Rev. Lett. **73**, 142 (1994).
[45] G. B. Lesovik, Pis'ma Zh. Eksp. Teor. Fiz. **49**, 513 (1989) [JETP Lett. **49**, 513 (1989)].
[46] M. Büttiker, Phys. Rev. B **46**, 12485 (1992).
[47] Y. M. Blanter and M. Büttiker, Phys. Rep. **336**, 1 (1999).
[48] C. Beenakker and C. Schönenberger, Phys. Today **56**, 37 (2006).
[49] S. Oberholzer, E. V. Sukhorukov, and C. Schönenberger, Nature (London) **415**, 765 (2002).
[50] O. Agam, I. Aleiner, and A. Larkin, Phys. Rev. Lett. **85**, 3153 (2000).
[51] H. S. Sim and H. Schomerus, Phys. Rev. Lett. **89**, 066801 (2002).
[52] C. W. J. Beenakker and H. van Houten, Phys. Rev. B **43**, 12066(R) (1991).
[53] F. Aigner, S. Rotter, and J. Burgdörfer, Phys. Rev. Lett. **94**, 216801 (2005).
[54] S. Datta and B. Das, Appl. Phys. Lett. **56**, 665 (1990).
[55] E. N. Bulgakov and A. F. Sadreev, J. Exp. Theor. Phys. Lett **73**, 505 (2001).
[56] E. Tsitsishvili, G. S. Lozano, and A. O. Gogolin, Phys. Rev. B **70**, 115316 (2004).
[57] F. Mireles and G. Kirczenow, Phys. Rev. B **64**, 024426 (2001).
[58] J. Wang, H. B. Sun, and D. Y. Xing, Phys. Rev. B **69**, 085304 (2004).
[59] A. A. Kiselev and K. W. Kim, Phys. Rev. B **61**, 13115 (2000).
[60] M. H. Liu and C. R. Chang, Phys. Rev. B **74**, 195314 (2006).
[61] J. A. Méndez-Bermúdez, G. A. Luna-Acosta, P. Šeba, and K. N. Pichugin, Phys. Rev. E **66**, 046207 (2002).
[62] J. D. Meiss, J. R. Cary, C. Grebogi, J. D. Crawford, A. N. Kaufman, and H. D. I. Abarbanel, Physica D **6**, 375 (1983).
[63] B. V. Chirikov and D. L. Shepelyansky, Physica D **13**, 395 (1984).
[64] J. D. Meiss and E. Ott, Phys. Rev. Lett. **55**, 2741 (1985).
[65] Y.-C. Lai, C. Grebogi, R. Blümel, and M. Ding, Phys. Rev. A **45**, 8284 (1992).
[66] Y.-C. Lai, M. Ding, C. Grebogi, and R. Blümel, Phys. Rev. A **46**, 4661 (1992).
[67] D. M. Zumbühl, J. B. Miller, C. M. Marcus, D. Goldhaber-Gordon, J. S. Harris, K. Campman, and A. C. Gossard, Phys. Rev. B **72**, 081305 (2005).
[68] İ. Adagideli, P. Jacquod, M. Scheid, M. Duckheim, D. Loss, and K. Richter, Phys. Rev. Lett. **105**, 246807 (2010).

[69] E. N. Bulgakov and A. F. Sadreev, Phys. Rev. E **70**, 056211 (2004).
[70] A. T. Ngo, E. H. Kim, and S. E. Ulloa, Phys. Rev. B **84**, 155457 (2011).
[71] O. Zaitsev, D. Frustaglia, and K. Richter, Phys. Rev. Lett. **94**, 026809 (2005).
[72] K.-F. Berggren and T. Ouchterlony, Found. Phys. **31**, 233 (2001).
[73] J. Cserti, A. Csordás, and U. Zülicke, Phys. Rev. B **70**, 233307 (2004).
[74] D. V. Khomitsky, A. I. Malyshev, E. Y. Sherman, and M. Di Ventra, Phys. Rev. B **88**, 195407 (2013).
[75] Y.-C. Lai, H.-Y. Xu, L. Huang, and C. Grebogi, Chaos **28**, 052101 (2018).
[76] L. Huang, H.-Y. Xu, C. Grebogi, and Y.-C. Lai, Phys. Rep. **753**, 1 (2018).